Can DNA-Protein Crosslinking Be Induced by One-Electron Oxidation of 8-Oxoguanine? A Model Study of 9-Methyl-8-oxoguanine Radical Cation with Methylamine

Wenjing Zhou,[a,b,c] Liang Feng,[a,b] May Myat Moe, [a,b] Johnny Ceballos,[a] Midas Tsai,[d] and Jianbo Liu*[a,b]

[a] Department of Chemistry and Biochemistry, Queens College of the City University of New York, 65-30 Kissena Blvd., Queens, NY 11367, USA; [b] Ph.D. Program in Chemistry, The Graduate Center of the City University of New York, 365 5th Ave., New York, NY 10016, USA; [c] Department of Natural Sciences, Morningside University, 1501 Morningside Avenue, Sioux City, Iowa 51106; and [d] Department of Natural Sciences, LaGuardia Community College, 31-10 Thomson Ave., Long Island City, NY 11101, USA

Abstract 8-oxoguanine (OG) is a common form of DNA damage and is itself more susceptible to further oxidative transformations. The oxidized OG derivatives can covalently bond with nucleophilic amino acid residues, contributing to DNA-protein crosslinks (DPCs). Previous research in this context focused on the reactivity of two-electron oxidized OG intermediate, 2-amino-7,9-dihydro-purine-6,8-dione (OG^{OX}), toward nucleophilic addition. In contrast, the role of one-electron oxidized OG radical cations ($OG^{\bullet+}$) remains unexplored. Herein we investigate a model system using 9-methyl-8-oxoguanine radical cation ($9MOG^{\bullet+}$) as an analogue of OG nucleoside and CH_3NH_2 as a mimic for the lysine ε-amine. The reaction of $9MOG^{\bullet+}$ with methylamine was measured across a range of kinetic energy in the gas phase by guided-ion-beam mass spectrometry. Density functional theory and DLPNO-CCSD(T) quantum chemistry computations were performed to elucidate reaction pathways and structures. Our results reveal that at low reaction energies, DPCs occur through direct nucleophilic addition, yielding C2-$^{+}NH_2CH_3[9MOG]^{\bullet}$ and C4-$^{+}NH_2CH_3[9MOG]^{\bullet}$. At high energies, DPCs become possible between protonated $[9MOG + H]^+$ and $^{\bullet}CH_2NH_2$/$^{\bullet}NHCH_3$ generated from hydrogen abstraction. This work provides insights into the distinct roles of one- versus two-electron oxidized OG species in DPC formation, expanding knowledge of OG lesions and their biological consequences.

Keywords: DNA-protein crosslinks, mass spectrometry, methylamine, nucleophilic addition, 8-oxoguanine radical cation

* E-mail: jianbo.liu@qc.cuny.edu. Tel: 1-718-997-3271.

1. Introduction

DNA–protein crosslinks (DPCs) are cytotoxic DNA lesions in which proteins become covalently tethered to DNA,[1] thereby obstructing cellular processes such as replication, transcription, and repair. The persistence of DPCs threatens genomic integrity,[2] leading to mutagenic outcomes and underscoring their significance in both toxicological and biomedical contexts. Despite their ubiquity, DPCs remain among the least understood forms of DNA damage, largely due to their diverse origins and complex formation pathways triggered by endogenous oxidative stress and exogenous agents.[3]

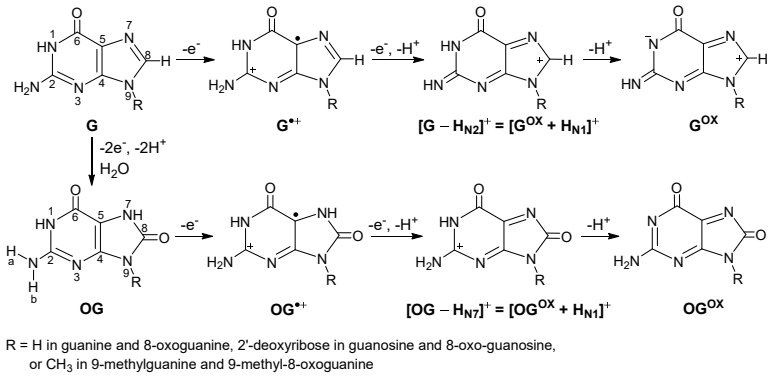

Scheme 1. One- and two-electron oxidation of guanine (G) and 8-oxoguanine (OG).

Guanine radical cations ($G^{\bullet+}$)[4-9] and two-electron oxidized guanine derivative (G^{OX})[10-12] in Scheme 1 are two DPC mediators identified by experiments[4-12] and theoretical studies.[12-18] 8-Oxoguanine (OG, Scheme 1),[19-21] resulting from oxidation and subsequent hydration of guanine, is another prominent DNA damage implicated in DPC formation. The abundance of OG lesion is 0.3 – 4.2 per 10^6 guanines in human lymphocyte DNA.[22] Due to its markedly lower oxidation potential ($E°$ = 0.74 V *vs.* NHE)[23] than canonical nucleobases (G: 1.29 V, A: 1.42 V, C: 1.6 V, and T: 1.7 V),[24, 25] OG is highly susceptible to further DNA oxidation.[7, 10, 26-28] Nucleophilic addition[7, 11, 15, 16, 29, 30] was detected between the two-electron oxidized quinonoid intermediate of OG, 2-amino-7,9-dihydro-purine-6,8-dione (OG^{OX}),[10, 26, 31] and protein nucleophiles, such as the ε-amine of lysine,[11, 32-34] arginine,[32] and tyrosine.[33, 35] This leads to crosslinking of OG^{OX}-containing DNA with *E. coli* single-stranded binding protein,[32] histone mutants within nucleosome core particles,[36] tris(hydroxymethyl)aminomethane,[37] and biogenic polyamines.[29]

In contrast, the involvement of one-electron oxidized OG radical cations ($OG^{\bullet+}$) in DPC formation remains poorly characterized, with few studies reported to date. Burrows and co-workers demonstrated that Ir^{4+}-mediated one-electron oxidation induced crosslinking between OG and lysine-142 of the *E. coli* MutY repair enzyme.[38] Although this DPC was initially attributed to $OG^{\bullet+}$ intermediacy, subsequent analysis pointed to the formation of a guanidinohydantoin-like adduct.[32]

Given that $OG^{\bullet+}$ acts as a global hole sink in oxidized DNA,[19, 23, 39, 40] it is pertinent to explore alternative DPCs mediated directly by $OG^{\bullet+}$. To this end, we employed a model system comprising 9-methyl-8-oxoguanine radical cation ($9MOG^{\bullet+}$, see Scheme 1) and methylamine. Our previous work[41] indicates that $9MOG^{\bullet+}$ is a reliable prototype for simulating $OG^{\bullet+}$ nucleoside chemistry, while also providing significant experimental convenience (higher ion intensity, improved mass resolution, and less ambiguities in mass spectrometry) and computational advantages (enabling the use of higher-level theories and more extensive basis sets). Methylamine (CH_3NH_2) was selected for modeling the DPC chemistry of ε-NH_2 in lysine (NH_2-CH(COOH)-$CH_2CH_2CH_2CH_2$-NH_2) for its $E°$ comparable to that of lysine.[42] It is noteworthy that ionization increases OG acidity (pK_{a1} = 8.6 for OG[43] *vs*. 6.6 for $OG^{\bullet+}$[23]). Consequently, 72% of free $OG^{\bullet+}$ deprotonates under neutral conditions to yield $[OG - H_{N7}]^{\bullet}$. In duplex DNA, however, N7-H can be stabilized through *syn-anti*-type mispairing with the N1 of A, O2 of T, O6 of G, or N3 of C.[44] To mimic cationic $OG^{\bullet+}$-induced DPC formation in DNA, we sought to investigate the crosslinking reactivity of $9MOG^{\bullet+}$ in the gas phase.

As demonstrated in our recent work,[12] gas-phase studies circumvent deprotonation and other solution-phase complexities and interferences, enabling observation of intrinsic reactivities and elementary steps. Moreover, nucleobase radical cations exhibit extended lifetimes in the gas phase, facilitating mechanistic interrogation. In the present study, we provide direct experimental and theoretical evidence for $OG^{\bullet+}$-mediated DPCs. The findings broaden the mechanistic framework of DPC formation and highlight the multifaceted oxidation chemistry of OG, with important implications for genomic stability and cellular health.

2. Results and Discussion

2.1. Reaction Products Between 9MOG$^{\bullet+}$ and Methylamine

The reaction was examined over a range of center-of-mass collision energy (E_{CM}) using guided-ion-beam mass spectrometry,[45] and 0.05 eV was chosen as the lowest energy to represent biologically relevant thermal (room temperature) conditions. To distinguish between different hydrogen abstraction pathways, isotopically labeled CD_3NH_2 was utilized as the neutral reactant. The occurrence of hydrogen/deuterium exchange between reactants also serves as a diagnostic marker for complex-mediated processes and their operative energy regime. Figure 1 presents product-ion mass spectra acquired at E_{CM} = 0.05, 0.5, and 1.5 eV, illustrating the product evolution across varying energy regimes.

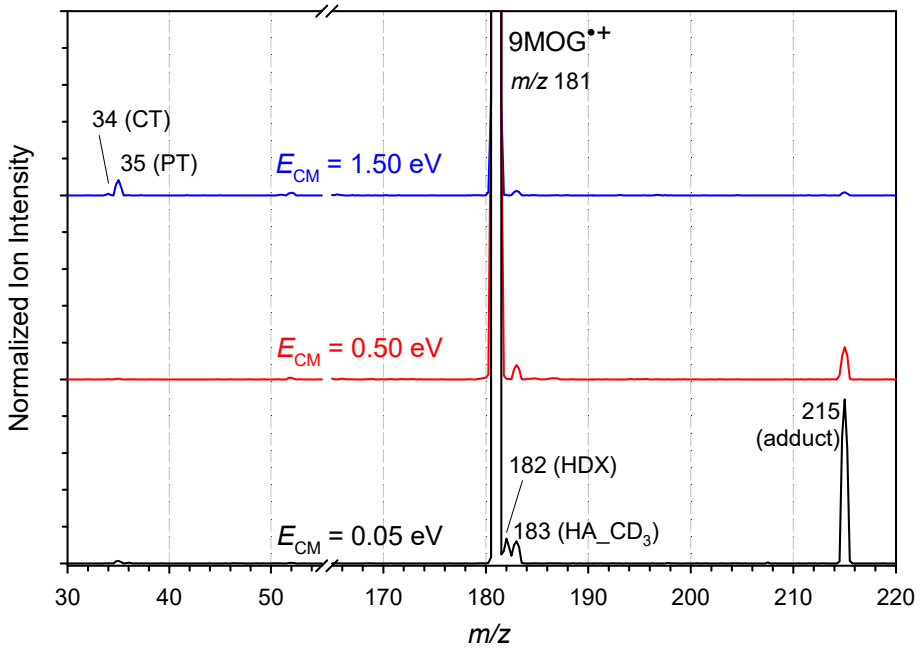

Figure 1. Product-ion mass spectra for the reaction of 9MOG$^{\bullet+}$ with CD_3NH_2 at E_{CM} = 0.05, 0.50, and 1.50 eV. Primary ion intensities were normalized to unit for comparison.

Prominent product ions were detected at *m/z* 34, 35, 182, 183, and 215, each corresponding to unique product channel(s) described below. Reaction enthalpies (ΔH, at 0 K) for charge- and proton-transfer processes were determined using a combination of reported experimental data and *ab initio* calculations:

***m/z* 34**	$CD_3NH_2^{\bullet+}$ + 9MOG	charge transfer (CT)	ΔH(0 K) = 1.67 eV
***m/z* 35**	$CD_3NH_3^+$ + [9MOG – H]$^\bullet$	proton transfer (PT)	ΔH(0 K) = 0.56 – 0.76 eV
***m/z* 182**	d_1-9MOG$^{\bullet+}$ + CHD_2NH_2	H/D exchange (HDX)	ΔH(0 K) = 0.00 eV
	or [9MOG + H]$^+$ + $CD_3NH^\bullet$	amine-H abstraction (HA_NH_2)	
***m/z* 183**	[9MOG + D]$^+$ + $^\bullet CD_2NH_2$	methyl-H abstraction (HA_CD_3)	
***m/z* 215**	[9MOG-NH_2CD_3]$^{\bullet+}$	crosslinking	

Figure 2 plots individual product cross sections as a function of E_{CM} over the range of 0.05 – 2.5 eV, where error bars represent standard deviations from three or more independent measurements.

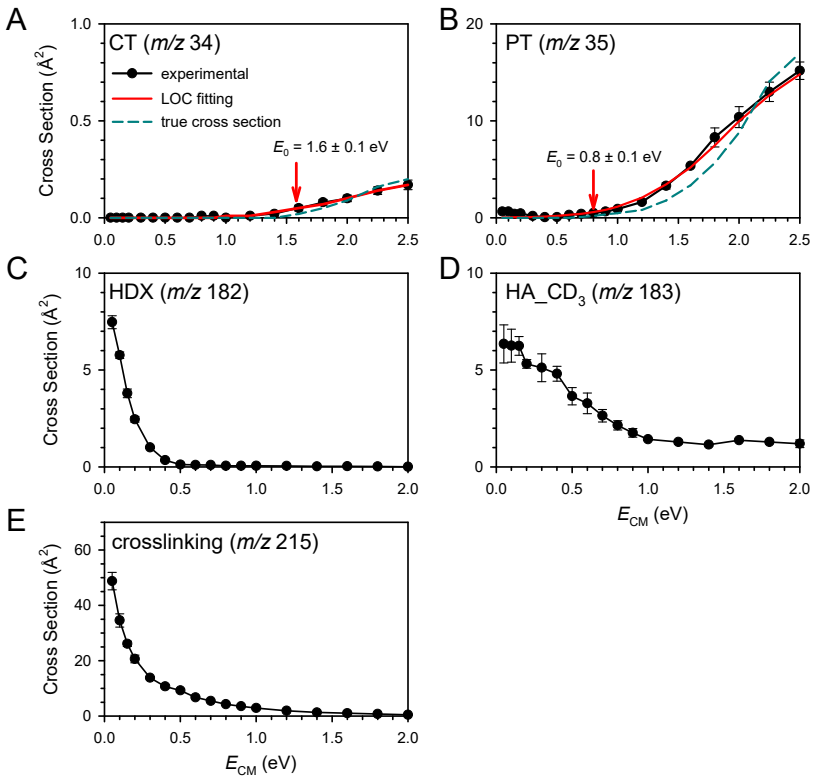

Figure 2. Individual product cross sections vs. E_{CM}. Black plots represent experimental data, red curves show LOC fits, and cyan dashed lines denote true cross sections without energy broadening.

Charge and proton transfer. Both channels exhibit threshold behavior, with cross sections rising from zero as E_{CM} increases (Figure 2A – B). Threshold energies (E_0, at 0 K) were extracted by fitting cross sections using a modified line-of-center (LOC) model,[46, 47] as shown by red solid lines (LOC fits) and cyan dashed lines (intrinsic cross sections corrected for kinetic energy broadening). The fits yielded E_0 values of 1.6 ± 0.1 eV (CT) and 0.8 ± 0.1 eV (PT), with uncertainties arising from the spread in experimental E_{CM}.

The experimental adiabatic ionization energy (AIE) for CH_3NH_2 is 9.04 eV.[48] No experimental AIE is available for 9MOG. DLPNO-CCSD(T)[49]/aug-cc-pVQZ//ωB97XD/6-31+G(d,p) calculations predict AIE(9MOG) = 7.37 eV. The same method gives an AIE of 7.78 eV for guanine (within 0.03 eV of photoionization data[50]), thereby validating computational accuracy. The resulting ΔH(0 K) for CT = AIE(CH_3NH_2) – AIE(9MOG) = 1.67 eV aligns well with the experimental E_0.

Gas-phase acidities for 9MOG$^{\bullet+}$, computed at the same level, are 9.89 eV (N1-H), 9.88 eV (N2-H_a), 10.08 eV (N2-H_b), and 9.92 eV (N7-H). The proton affinity of CH_3NH_2 is 9.32 eV.[51] These values predict a ΔH range of 0.56 – 0.76 eV for PT, consistent with the experimental E_0 of 0.8 ± 0.1 eV. Note under physiological conditions DNA frequently encounters cationic ammonium species;[17] formation of deprotonated [9MOG – H]$^{\bullet}$ therefore reduces electrostatic repulsion for close-range reactivity.

Isotope scrambling pinpoints complex-mediated regime. Product ions at *m/z* 182 may arise from H/D exchange and/or H abstraction from the amine group of CD_3NH_2 by 9MOG$^{\bullet+}$ (HA_NH_2). These pathways differ in energy dependence. H/D exchange is thermoneutral and follows an ion–dipole capture profile[52] that maximizes at low E_{CM} and decreases with increasing E_{CM}. In contrast, HA_NH_2 pathways are computed to be endothermic (*vide infra*), with cross section expected to increase at higher E_{CM}. The energy profile of *m/z* 182 (Figure 2C) supports its origin from H/D exchange. The fact that H/D exchange ceases at 0.5 eV, marking a shift for the system from complex-mediated to direct dynamics.

Hydrogen abstraction from methyl. As shown in Figure 2D, the cross section for product *m/z* 183 peaks at 6.5 Å^2 at 0.05 eV, declines to 3.6 Å^2 at 0.5 eV, and plateaus around 1.2 Å^2 at higher E_{CM}. Given that the single H/D exchange cross section falls to 0.1 Å^2 at 0.5 eV, the *m/z* 183 profile reveals two points. First, the product is dominated by methyl-H abstraction from CD_3NH_2 (HA_CD_3) over a broad E_{CM} range, whereas any contributions of double H/D exchange to *m/z* 183 are expected only below 0.5 eV. Secondly, HA_CD_3 presents a dual character: low-energy reactivity points to complex-mediation; high-energy favors direct abstraction.

Crosslinking represents the dominant reaction outcome. The cross section (*m/z* 215) for methylamine

addition to 9MOG$^{\bullet+}$ reaches 49 Å^2 at the lowest E_{CM} and persists up to 1.5 eV (Figure 2E). The broad energy range for crosslinking also reflects contributions from two regimes: low-energy (at E_{CM} < 0.5 eV) complex-mediated interaction characterized by extended interaction time and enhanced probability, and high-energy direct mechanisms where increased kinetic energy overcomes orientation and activation barriers, enabling barrier-limited bond formation. The dual mechanism is reinforced by crosslinking branching ratio shown in Figure 3A. Crosslinking predominates in the 0.05 – 1.0 eV range with ratio ≥ 0.5. Beyond 1.0 eV, the ratio drops quickly, consistent with the onset of competing PT.

Total product cross sections (σ_{total}) is presented in Figure 3B, which peaks at 64 Å^2 at the lowest E_{CM}, decrease to 5 Å^2 near 1.2 eV, and rises moderately at higher E_{CM}. Reaction efficiency was calculated as $\sigma_{total}/\sigma_{collision}$, where $\sigma_{collision}$ was taken as the greater of two values: statistical adiabatic ion–neutral capture cross section (representing unity reaction probability once long-range electrostatic attraction brings reactants within capture distance),[52] and hard-sphere collision cross section derived from the orientation-averaged projected area of reactants (serving as a geometric baseline).[53, 54] The efficiency reaches 30% at 0.1 eV, decreases to a minimum of 5.7% at 1.2 eV, and recovers to 14% at 2.0 eV. The dip at 0.05 eV was due to the loss of back-scattered product ions within the octopole ion guide[45] at the lowest E_{CM}.

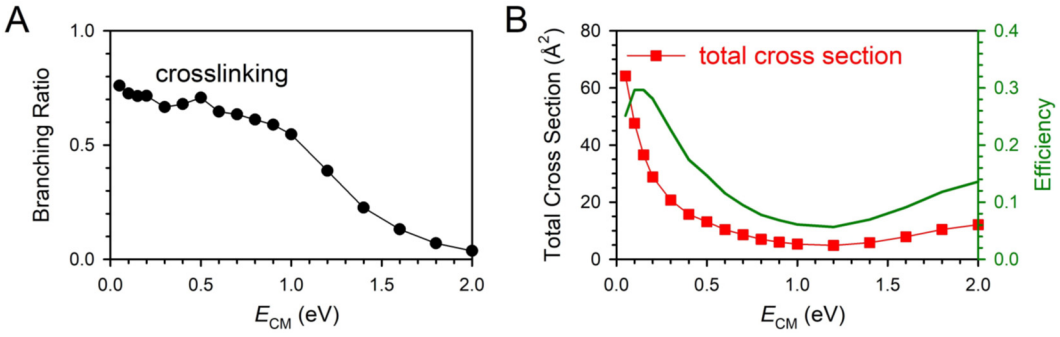

Figure 3. (**A**) Branching ratio for crosslinking and (**B**) total product cross section and reaction efficiency (green line, right axis) as a function of E_{CM}.

2.2. Crosslinking Pathways, Structures, and Energetics

To identify crosslinking pathways and structures in the experiment, we explored reaction coordinates for 9MOG$^{\bullet+}$ + CH_3NH_2 systematically using density functional theory (DFT) ωB97XD/6-31+G(d,p).

This functional incorporates long-range dispersion corrections and reduces self-interaction errors, accurately describing radical orbitals and non-covalent interactions.[55] Electronic energies were refined via single-point calculations at the domain-based local pair-natural orbital coupled cluster level with single-, double-, and perturbative triple excitations, DLPNO-CCSD(T)[49]/aug-cc-pVQZ. A total of 620 reaction structures were computed. Energy differences between DFT and CCSD(T) results are typically < 0.1 eV, confirming the robustness of computed trends.

2.2.1. Formation of X-$^{+}NH_2CH_3$[9MOG]$^{\bullet}$ via direct nucleophilic addition. Calculations suggest that direct N-terminal methylamine addition to 9MOG$^{\bullet+}$ is possible at multiple positions, except N2, C5, C6, N7, and N9 which involves alternative mechanisms discussed below. The X-$^{+}NH_2CH_3$[9MOG]$^{\bullet}$ products (X = N1, C2, N3, C4, O6, C8, and O8) are shown in Scheme 2, together with reaction enthalpies and activation barriers at transition states (TSs). Cartesian coordinates for adducts and TSs are provided in Supporting Information.

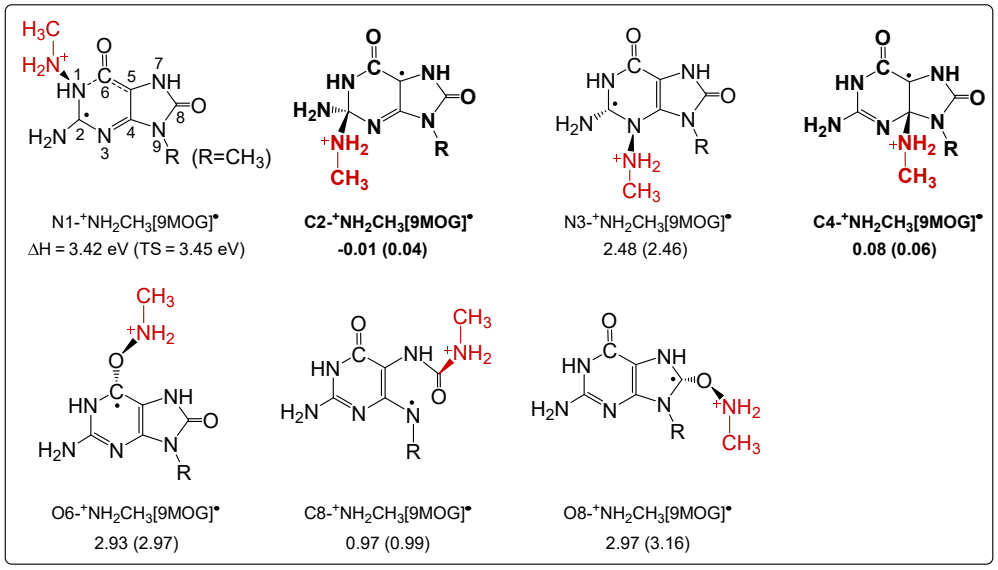

Scheme 2. Direct N-terminal addition of CH_3NH_2 to 9MOG$^{\bullet+}$. Reaction ΔH(298K) and activation barriers (in parentheses) were computed at the DLPNO-CCSD(T)/aug-cc-pVQZ level. Structures in bold denote probable low-energy crosslinks in the experiment.

Most direct addition pathways are endothermic with substantial barriers. Only C2- and C4-addition in reactions (1.1 – 2) are thermoneutral and nearly barrierless, suggesting their contributions to the

experimental adducts at low E_{CM} (Figure 2E). The resulting C2-$^{+}NH_2CH_3$[9MOG]$^{\bullet}$ and C4-$^{+}NH_2CH_3$[9MOG]$^{\bullet}$ are highlighted in Scheme 2. For C4 addition, the TS electronic energy is marginally higher than that of product. Because one vibrational mode has converted to the reaction coordinate in addition and was excluded in thermal correction, the ΔH(298 K) of the TS falls slightly below the product. Finally, formation of C8-$^{+}NH_2CH_3$[9MOG]$^{\bullet}$ in reaction (1.3) may occur at moderate E_{CM}.

$$9MOG^{\bullet+} + CH_3NH_2 \rightarrow$$

$$C2\text{-}{}^{+}NH_2CH_3[9MOG]^{\bullet} \quad \Delta H/TS = -0.01/0.04 \text{ eV} \quad (1.1)$$

$$C4\text{-}{}^{+}NH_2CH_3[9MOG]^{\bullet} \quad \Delta H/TS = 0.08/0.06 \text{ eV} \quad (1.2)$$

$$C8\text{-}{}^{+}NH_2CH_3[9MOG]^{\bullet} \quad \Delta H/TS = 0.97/\ 0.99 \text{ eV} \quad (1.3)$$

2.2.2. Formation of X-NHCH$_3$[9MOG + H]$^{\bullet+}$ via stepwise and concerted mechanisms. X-NHCH$_3$[9MOG + H]$^{\bullet+}$ adducts can form through multiple pathways, summarized in Scheme S1 and Table S1 in Supporting Information. For clarity, they are grouped by the methylamine addition site; and each site is further categorized into five mechanisms:

1) Intramolecular PT from the $^{+}NH_2CH_3$ group to the 9MOG scaffold within primary X-$^{+}NH_2CH_3$[9MOG]$^{\bullet}$ adducts, yielding isomeric products, such as reaction (2.1):

$$9MOG^{\bullet+} + CH_3NH_2 \rightarrow C2\text{-}{}^{+}NH_2CH_3[9MOG]^{\bullet} \rightarrow C2\text{-}NHCH_3[9MOG + H_{N2}]^{\bullet+} \quad \Delta H/TS = 0.24/1.11 \text{ eV} \quad (2.1)$$

2) Asynchronous concerted addition and PT, wherein methylamine addition to 9MOG$^{\bullet+}$ and PT from the amine group proceed through a single TS but the addition precedes PT. A representative case is reaction (2.2), which becomes relevant at moderately high energies, despite the C1-N6 bond being ruptured in the adduct (see structure in Scheme S1)

$$9MOG^{\bullet+} + CH_3NH_2 \rightarrow C6\text{-}NHCH_3[9MOG + H_{N1}]^{\bullet+} \quad \Delta H/TS = -0.69/0.84 \text{ eV} \quad (2.2)$$

3) Synchronous concerted addition and PT, wherein two events occur simultaneously, *e.g.*

$$9MOG^{\bullet+} + CH_3NH_2 \rightarrow C6\text{-}NHCH_3[9MOG + H_{O6}]^{\bullet+} \quad \Delta H/TS = -0.28/1.16 \text{ eV} \quad (2.3)$$

The asynchronous and synchronous concerted mechanisms enable addition to the sites (N2, C5, C6, N7, and N9) that are otherwise inaccessible via direct addition.

4) Crosslinking following amine-H abstraction. Reactions (2.4 – 2.14) summarize computed amine-H

abstraction pathways. HA_NH_2 by C8 was not considered as the reaction would rupture the imidazole ring, and its primary products are unlikely to undergo a crosslinking reaction.

$9MOG^{\bullet+} + CH_3NH_2 \rightarrow$

$[9MOG + H_{N1}]^+\cdots {}^{\bullet}NHCH_3$ $\Delta H/TS = 1.93/2.13$ eV $\rightarrow [9MOG + H_{N1}]^+ + {}^{\bullet}NHCH_3$ $\Delta H = 2.65$ eV (2.4)

$[9MOG + H_{C2}]^+ + {}^{\bullet}NHCH_3$ $\Delta H = 3.12$ eV (2.5)

$[9MOG + H_{N2}]^+ + {}^{\bullet}NHCH_3$ $\Delta H = 2.33$ eV (2.6)

$[9MOG + H_{N3}]^+\cdots {}^{\bullet}NHCH_3$ $\Delta H/TS = 0.41/0.56$ eV $\rightarrow [9MOG + H_{N3}]^+ + {}^{\bullet}NHCH_3$ $\Delta H = 1.37$ eV (2.7)

$[9MOG + H_{C4}]^+\cdots {}^{\bullet}NHCH_3$ $\Delta H/TS = 2.09/2.26$ eV $\rightarrow [9MOG + H_{C4}]^+ + {}^{\bullet}NHCH_3$ $\Delta H = 2.62$ eV (2.8)

$[9MOG + H_{C5}]^+\cdots {}^{\bullet}NHCH_3$ $\Delta H/TS = 0.71/1.01$ eV $\rightarrow [9MOG + H_{C5}]^+ + {}^{\bullet}NHCH_3$ $\Delta H = 1.16$ eV (2.9)

$[9MOG + H_{C6}]^+\cdots {}^{\bullet}NHCH_3$ $\Delta H/TS = 1.55/3.45$ eV $\rightarrow [9MOG + H_{C6}]^+ + {}^{\bullet}NHCH_3$ $\Delta H = 2.27$ eV (2.10)

$[9MOG + H_{O6}]^+\cdots {}^{\bullet}NHCH_3$ $\Delta H/TS = -0.01/0.07$ eV$\rightarrow [9MOG + H_{O6}]^+ + {}^{\bullet}NHCH_3$ $\Delta H = 1.00$ eV (2.11)

$[9MOG + H_{N7}]^+ + {}^{\bullet}NHCH_3$ $\Delta H = 1.79$ eV (2.12)

$[9MOG + H_{O8}]^+\cdots {}^{\bullet}NHCH_3$ $\Delta H/TS = 0.01/-0.07$ eV $\rightarrow [9MOG + H_{O8}]^+ + {}^{\bullet}NHCH_3$ $\Delta H = 1.13$ eV (2.13)

$[9MOG + H_{N9}]^+ + {}^{\bullet}NHCH_3$ $\Delta H = 2.03$ eV (2.14)

The $\Delta H(298K)$ values for separated HA products range from 1.00 to 3.12 eV, suggesting HA_NH_2 could not contribute to the *m/z* 182 products (that were detected only at $E_{CM} < 0.5$ eV). The significance of HA_NH_2, however, lies in the formation of product-like intermediates $[9MOG + H]^+\cdots {}^{\bullet}NHCH_3$. For example, reactions (2.11) and (2.13) produce thermoneutral $[9MOG + H_{O6}]^+\cdots {}^{\bullet}NHCH_3$ and $[9MOG + H_{O8}]^+\cdots {}^{\bullet}NHCH_3$ with negligible barriers, suggesting their relevance in low-energy, non-covalent adduct formation. More importantly, these product-like intermediates may recombine into covalently bonded $NHCH_3[9MOG + H]^{\bullet+}$ adducts, as presented in Table S1 and Scheme S1. Among these, formation of C6-$NHCH_3[9MOG + H_{O6}]^{\bullet+}$ in reaction (2.15) is a probable contribution to experimental crosslinks:

$9MOG^{\bullet+} + CH_3NH_2 \rightarrow [9MOG + H_{O6}]^+\cdots {}^{\bullet}NHCH_3 \rightarrow$ C6-$NHCH_3[9MOG + H_{O6}]^{\bullet+}$ $\Delta H/TS = -0.28/0.99$ eV (2.15)

5) Asynchronous HA_NH_2 and addition. As shown in reactions (2.5), (2.6), (2.12) and (2.14), products from HA_NH_2 by C2, N2, N7, and N9 could not form a non-covalent intermediate; but the system may accompany HA_NH_2 with asynchronous N-terminal addition of nascent ${}^{\bullet}NHCH_3$ within a single TS. These pathways are indicated as "*async* HA_NH_2 + add" in Table S1, albeit being more energy demanding and less likely to occur in the experiment.

Tabel S1 and Scheme S1 compare different pathways leading to the same X-$NHCH_3[9MOG + H]^{\bullet+}$

isomer. While crosslinking pathways following HA_NH_2 are more versatile and generate more isomers, no single type of mechanism dominates kinetically or thermodynamically. Most X-$NHCH_3$[9MOG + H]$^{\bullet+}$ adducts adopt a distonic structure with separated charge and spin. However, C2-$^{+}\dot{N}HCH_3$[9MOG + $H_{C5/C6}$], C4-$^{+}\dot{N}HCH_3$[9MOG + $H_{C5/O6}$], and C5-$^{+}\dot{N}HCH_3$[9MOG + $H_{C2/C4}$] localize both charge and unpaired electron on the amine N-atom. Finally, C2-, C4-, C5- and C6-$NHCH_3$[9MOG + H]$^{\bullet+}$ are more stable compared to their N1-, N2-, N3-, O6-, N7-, C8-, O8-, and N9-analogues.

2.2.3. Formation of X-CH_2NH_2[9MOG + H]$^{\bullet+}$ following methyl-H (HA_CH_3) and methyl-H$^-$ abstraction (H⊖A_CH_3). Reactions (3.1), (3.3), (3.5) and (3.6 – 11) represent HA_CH_3. Reactions (3.2) and (3.4) correspond to H⊖A_CH_3. For the same reason as HA_NH_2, HA_CH_3 by C8 was excluded.

$9MOG^{\bullet+} + CH_3NH_2 \rightarrow$

$[9MOG + H_{N1}]^{+}\cdots {}^{\bullet}CH_2NH_2$ ΔH/TS = 1.60/1.59 eV → $[9MOG + H_{N1}]^{+} + {}^{\bullet}CH_2NH_2$ ΔH = 2.37 eV (3.1)

$[9MOG + H_{C2}]^{\bullet}\cdots {}^{+}CH_2NH_3$ ΔH/TS = 0.48/1.60 eV → $[9MOG + H_{C2}]^{\bullet} + {}^{+}CH_2NH_2$ ΔH = 1.76 eV (3.2)

$[9MOG + H_{N2}]^{+}\cdots {}^{\bullet}CH_2NH_2$ ΔH/TS = 1.15/1.18 eV → $[9MOG + H_{N2}]^{+} + {}^{\bullet}CH_2NH_2$ ΔH = 2.05 eV (3.3)

$[9MOG + H_{N3}]^{+}\cdots {}^{\bullet}CH_2NH_2$ ΔH/TS = 0.53/0.83 eV → $[9MOG + H_{N3}]^{+} + {}^{\bullet}CH_2NH_2$ ΔH = 1.09 eV (3.4)

$[9MOG + H_{C4}]^{\bullet}\cdots {}^{+}CH_2NH_3$ ΔH/TS = 0.61/1.47 eV → $[9MOG + H_{C4}]^{\bullet} + {}^{+}CH_2NH_2$ ΔH = 1.75 eV (3.5)

$[9MOG + H_{C5}]^{+}\cdots {}^{\bullet}CH_2NH_2$ ΔH/TS = 0.49/0.56 eV → $[9MOG + H_{C5}]^{+} + {}^{\bullet}CH_2NH_2$ ΔH = 0.88 eV (3.6)

$[9MOG + H_{C6}]^{+}\cdots {}^{\bullet}CH_2NH_2$ ΔH/TS = 1.48/1.87 eV → $[9MOG + H_{C6}]^{+} + {}^{\bullet}CH_2NH_2$ ΔH = 2.00 eV (3.7)

$[9MOG + H_{O6}]^{+}\cdots {}^{\bullet}CH_2NH_2$ ΔH/TS = 0.09/0.28 eV → $[9MOG + H_{O6}]^{+} + {}^{\bullet}CH_2NH_2$ ΔH = 0.64 eV (3.8)

$[9MOG + H_{N7}]^{+} + {}^{\bullet}CH_2NH_2$ ΔH = 1.51 eV (3.9)

$[9MOG + H_{O8}]^{+}\cdots {}^{\bullet}CH_2NH_2$ ΔH/TS = 0.16/0.20 eV → $[9MOG + H_{O8}]^{+} + {}^{\bullet}CH_2NH_2$ ΔH = 0.85 eV (3.10)

$[9MOG + H_{N9}]^{+}\cdots {}^{\bullet}CH_2NH_2$ ΔH/TS = 1.11/1.02 eV → $[9MOG + H_{N9}]^{+} + {}^{\bullet}CH_2NH_2$ ΔH = 1.75 eV (3.11)

Natural bond orbital (NBO) analysis shows C2 and C4 carry charges of +0.680 and +0.466, respectively — higher than most atoms in 9MOG except C6 (+0.633) and C8 (+0.832), and the latter are shielded by the adjacent carbonyl O6 (-0.497) and O8 (-0.493). Furthermore, neither C2 nor C4 exhibits any spin density. These properties make their hydride abstraction possible. However, no H⊖A_CH_3 was observed in the experiment. The ΔH(298K) for HA_CH_3 was calculated to be 0.64 to 2.37 eV, with reaction (3.8) being the least endothermic. This is consistent with the broad E_{CM} range for HA_CD_3 products in Fig. 2D.

To determine relative importance of individual HA_CH_3 pathways, branching ratios were evaluated

using Rice-Ramsperger-Kessel-Marcus (RRKM) theory.[56] Kinetics modeling indicates methyl-H abstraction is dominated by O8 in reaction (3.10), followed by O6 in reaction (3.8), with minor contribution from C5 in reaction (3.6). Given the use of d_3-methylamine in the experiment, kinetic isotope effects (KIEs) for methyl-H abstraction from normal and C-deuterated methylamine were examined. The calculated k_H/k_D ratios for reactions (3.8) and (3.10) are 8 – 12 at 0.5 eV and 4 – 5 at 1.0 eV, suggesting that methyl-H abstraction is substantially enhanced in non-deuterated systems. Notably, large KIEs are common for radical-induced methyl-H abstraction, consistent with C-H bond cleavage being rate limiting. For example, pronounced KIEs have also been reported for H abstraction from methylamine by 9MG$^{\bullet+}$ (KIE = 4 – 5 in the gas phase)[12] and $^{\bullet}$OH (KIE = 1.86 in solution, with potentially large values in the gas phase).[57]

Tunneling contributions to H abstraction[57] was assessed using Wigner factor[58] $[1 + \frac{1}{24}\left(\frac{h\upsilon}{k_B T}\right)^2]$. TS imaginary frequency for reaction (3.6) is 276 cm^{-1} with CH_3NH_2 and 257 cm^{-1} with CD_3NH_2, yielding Wigner factors of 1.08 (CH_3NH_2) and 1.07 (CD_3NH_2). Wigner factors are 1.10 (CH_3NH_2) and 1.07 (CD_3NH_2) for reaction (3.8), and 1.05 (CH_3NH_2) and 1.04 (CD_3NH_2) for reaction (3.10). These tunneling factors are rather modest. Thus, the cross section for *m/z* 183 at the lowest E_{CM} (Figure 2D) reflects a combination of experimental energy broadening in cross sections, tunneling for HA_CD_3, and double H/D exchange.

Similar to the HA_NH_2 scenario, HA_CH_3 and H⊖A_CH_3 reactions can form non-covalent, product-like complexes before dissociating (except HA_CH_3 by N7), and crosslinking is possible within these complexes. For HA_CH_3 by N7, crosslinking occurs concerted with H abstraction. The resulting adduct structures and energetics are summarized in Scheme 3 as well as Scheme S2 and Table S2 in Supporting Information. Most of these crosslinking pathways yield X-CH_2NH_2[9MOG + H]$^+$ structures; but it is possible to form C5-$^+NH_2\dot{C}H_2$[9MOG + $H_{C2/C4}$] via N-terminal additions of $^{\bullet}CH_2NH_2$. Notably, many crosslinks following HA_CH_3 by O6 and O8 have barriers below 1.0 eV. These low-barrier adducts are presented in bold in Scheme 3 as they represent probable experimental crosslinks at high E_{CM}.

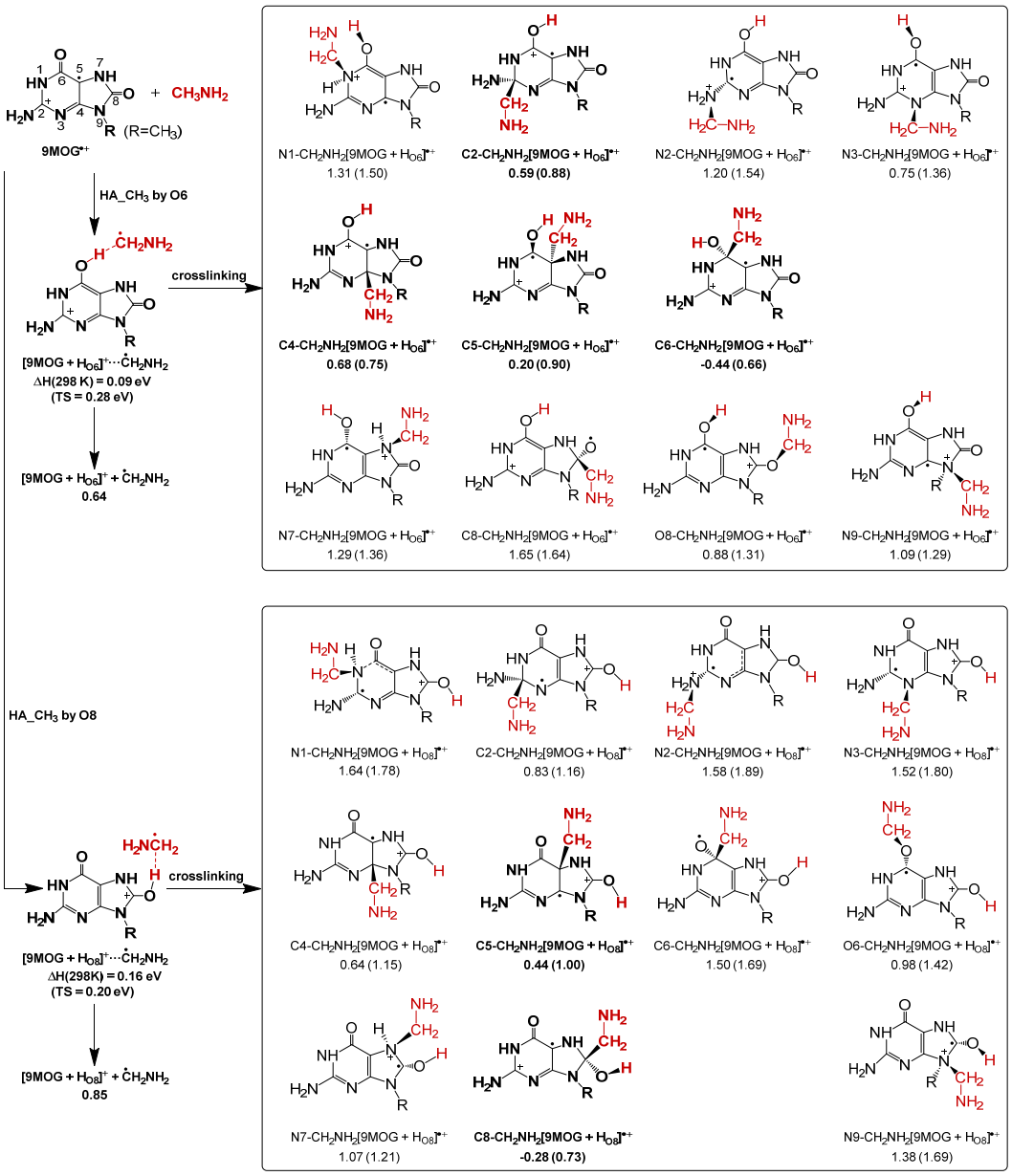

Scheme 3. Crosslinking following HA_CH_3 by O6 and O8 of $9MOG^{\bullet+}$. Reaction ΔH(298 K) and barriers (in parentheses) were calculated at DLPNO-CCSD(T)/aug-cc-pVQZ. Structures in bold represent probable high-energy crosslinks in the experiment.

2.3. Comparison of Crosslinking Mediated by One-Electron Oxidized Guanine and 8-Oxoguanine

This comparison is informative given that $G^{\bullet+}$ is recognized as one of key mediators for DPCs under oxidative DNA damage.[4-9] The crosslinking of $9MG^{\bullet+}$ with CD_3NH_2 has been previously examined over a wide E_{CM} range.[12] The total reaction efficiency is 7% at 0.05 eV, decreasing to 5% at 0.3 eV and remaining constant thereafter. The crosslinking branching ratio starts at 0.4 (0.05 eV), drops to 0.1 by 0.2

eV and approaches zero above 0.4 eV. Hence, the maximum crosslinking efficiency is about 3%, becoming negligible above 0.3 eV. In contrast, 9MOG$^{\bullet+}$ exhibits a crosslinking yield exceeding 19% at thermal energy, remaining ≥ 10 % up to 0.5 eV, 3% at 1.0 eV, and 0.5 % at 2.0 eV. This disparity highlights enhanced reactivity and crosslinking propensity of 9MOG$^{\bullet+}$ toward methylamine, attributed to the increased electrophilicity conferred by the 8-oxo substitution.

Table 1 summarizes mechanistic differences. For 9MG$^{\bullet+}$, crosslinking proceeds via direct N-terminal addition of methylamine and, more prominently, through covalent combination of [9MG + H]$^+$···$^\bullet$CH$_2$NH$_2$ formed by methyl-H abstraction. The rapid decline in crosslinking with increasing energy suggests a dominating complex-mediated mechanism. For 9MOG$^{\bullet+}$, low-energy crosslinking arises from N-terminal addition of CH$_3$NH$_2$, with added contributions from non-covalent association of abstraction products [9MOG + H]$^+$···$^\bullet$NHCH$_3$. At higher energies, crosslinking is mediated by combination of H-abstraction products, *i.e.*, [9MOG + H$_{O6}$]$^+$ and [9MOG + H$_{O8}$]$^+$ with $^\bullet$NHCH$_3$ and/or $^\bullet$CH$_2$NH$_2$. These pathways involve moderate barriers, with yields influenced by dynamics such as collision energy and orientations, rearrangement, and interaction time. Note in double-stranded DNA, O6 of OG is paired/mispaired with other nucleobases,[44] making X-NHCH$_3$[9MOG + H$_{O6}$]$^{\bullet+}$ and X-CH$_2$NH$_2$[9MOG + H$_{O6}$]$^{\bullet+}$ less accessible. Therefore, the X-CH$_2$NH$_2$[9MOG + H$_{O8}$]$^{\bullet+}$ adducts are more biologically relevant.

Table 1 Crosslinking of CH$_3$NH$_2$ with 9MOG$^{\bullet+}$ vs. 9MG$^{\bullet+}$

	thermal energy			high energy (0.5- 1.5 eV)		
	yield%	mechanisms	probable adducts	yield%	mechanisms	probable adducts
9MOG$^{\bullet+}$	19	direct addition (major)	X-$^+$NH$_2$CH$_3$[9MOG]$^\bullet$ (X = C2, C4)	0.5–10	*async* addition + PT	C6-NHCH$_3$[9MOG + H$_{N1}$]$^{\bullet+}$
		HA_NH$_2$-mediated	[9MOG + H$_X$]$^+$···$^\bullet$NHCH$_3$ (X = O6, O8)		HA_NH$_2$-mediated	C6-NHCH$_3$[9MOG + H$_{O6}$]$^{\bullet+}$
					HA_CH$_3$-mediated	X-CH$_2$NH$_2$[9MOG + H$_{O6}$]$^{\bullet+}$ (X = C2, C4, C5, C6)
						X-CH$_2$NH$_2$[9MOG + H$_{O8}$]$^{\bullet+}$ (X = C5, C8)
9MG$^{\bullet+}$	3	HA_CH$_3$-mediated (major)	C8-CH$_2$NH$_2$[9MG + H$_{N7}$]$^{\bullet+}$	none	N/A	N/A
		direct addition	X-NH$_2$CH$_3$[9MG]$^{\bullet+}$ (X = N2, C8)			

3. Conclusions

The reaction of 8-oxoguanine radical cation with methylamine was investigated across collision energies. Mechanistic insights were obtained through DFT and CCSD(T) calculations. Together with previous studies on guanine radical cation and two-electron oxidized OG^{OX}, these results reveal distinctive reactivities of guanine nucleobases during oxidative transformations. For $G^{\bullet+}$, DPCs occur primarily at C8, yielding the C8-$CH_2NH_2[G + H_{N7}]^{\bullet+}$ adduct. In contrast, $OG^{\bullet+}$ enables formation of C2-$^{+}NH_2CH_3[OG]^{\bullet}$ and C4-$^{+}NH_2CH_3[OG]^{\bullet}$ adducts at thermal energies. At elevated energies, crosslinking follows H-abstraction from methyl and amine group, yielding X-$NHCH_3[OG + H_{N1/O6}]^{\bullet+}$ and X-$CH_2NH_2[OG + H_{O6/O8}]^{\bullet+}$ adducts. Finally, for doubly oxidized OG^{OX}, DPCs occur preferentially at C5, forming 7H-C5-$NHCH_3[OG^{OX}]$. However, $OG^{\bullet+}$-derived DPC adducts are thermoneutral or energetically uphill, suggesting limited thermodynamic stability and potential for dissociation or conversion into downstream products – a hint for their inefficiency in biological systems.

4. Experimental and Computational Section

Experimental Methods. 9MOG was provided by Dr. Lippert (University of Dortmund, Germany).[59] 2′-Deoxyguanosine (dGuo, Sigma-Aldrich, > 99%), $Cu(NO_3)_2$ (Alfa Aesar, 99.999%), and CD_3NH_2 gas (Cambridge Isotope Laboratories, d_3 98%) were used as received. Experiments employed a home-built guided-ion-beam mass spectrometer[45] comprising an electrospray ionization source, radiofrequency (rf) hexapole ion guide, quadrupole mass filter for reactant ion selection, rf octopole ion guide with scattering cell, second quadrupole mass filter for product analysis, and a pulse-counting multiplier detector.

$9MOG^{\bullet+}$ was generated via redox dissociation $[Cu^{II}(9MOG)_3]^{\bullet2+} \rightarrow [Cu^{I}(9MOG)_2]^{+} + 9MOG^{\bullet+}$.[41, 60-63] A fresh solution containing equimolar concentrations (0.25 mM) of $Cu(NO_3)_2$, 9MOG, and dGuo (used to enhance redox separation[41]) in 3:1 methanol/water was electrosprayed into the mass spectrometer source chamber through a 190 °C desolvation capillary. A 1.0-mm-orifice skimmer is positioned 3 mm downstream from the capillary end. The electric field between the capillary and skimmer prompted dissociation of Cu^{II}-9MOG complexes by collisions with background gas (1.6 Torr) in

the source chamber, producing 9MOG$^{\bullet+}$ at 1.2×10^5 counts per sec. Ions were thermalized to 310 K via collisional cooling in the hexapole, mass-selected by the first quadrupole, and injected into the octopole containing CD_3NH_2 gas (0.01 mTorr). A DC bias upon the octopole controlled the laboratory-frame ion kinetic energy (E_{lab}), which converted to center-of-mass collision energy (E_{CM}) as $E_{CM} = E_{lab} \times m_{neutral\ gas} / (m_{ion} + m_{neutral\ gas})$. Energy spread in E_{CM} was ≤ 0.09 eV (FWHM). Product and unreacted reactant ions were analyzed by the second quadruple. Low reactant gas pressure ensured single ion-molecule collision conditions, enabling cross section measurements using the Beer–Lambert law.[64]

Threshold energies (E_0 at 0 K) for endothermic processes were extracted by fitting energy-dependent product cross sections using a modified line-of-centers (LOC) model:[46, 47] $\sigma(E_{CM}) = \sigma_0(E_{CM} + E_{vib} + E_{rot} - E_0)^n/E_{CM}$, where σ_0 is a normalization factor, E_{vib} and E_{rot} are vibrational and rotational energies of reactants, and n (= 2.4 – 3.8) describes the kinetic energy efficiency in reactions. A Monte Carlo ion-molecule collision program was incorporated into LOC fitting to simulate energy broadening arising from Boltzmann distributions of E_{vib} and E_{rot}, Doppler broadening,[65] and kinetic shift.[66]

Computational methods. Geometries of reactants, intermediates, TSs, and products were optimized at ωB97XD/6-31+G(d,p) using Gaussian 16.[67] Vibrational frequency analyses confirmed stable minima (no imaginary frequency) and TSs (single imaginary frequency). Intrinsic reaction coordinate calculations verified each TS connected correct reactant and product. Reaction ΔH includes zero-point energy (scaled by 0.975[68]) and thermal correction. Charge and spin were analyzed using NBO 6.0.[69] Electronic energies were refined at DLPNO-CCSD(T)[49]/aug-cc-pVQZ using ORCA 6.0.1.[70] RRKM[56] rate constants were computed using the Zhu-Hase code.[71]

Acknowledgement

This work was supported by National Science Foundation (Grant No. CHE 2350109).

Supporting Information

Reaction schemes, energetics, and Cartesian coordinates.

[1] N. Y. Tretyakova, A. Groehler, III, S. Ji, *Acc. Chem. Res.* **2015**, *48*, 1631.
[2] H. Ide, T. Nakano, A. M. H. Salem, M. I. Shoulkamy, *DNA Repair (Amst)* **2018**, *71*, 190.
[3] Y. Kojima, Y. J. Machida, *Environ. Mol. Mutagen.* **2020**, *61*, 716.
[4] B. Morin, J. Cadet, *J. Am. Chem. Soc.* **1995**, *117*, 12408.
[5] S. Perrier, J. Hau, D. Gasparutto, J. Cadet, A. Favier, J.-L. Ravanat, *J. Am. Chem. Soc.* **2006**, *128*, 5703.
[6] S. Silerme, L. Bobyk, M. Taverna-Porro, C. Cuier, C. Saint-Pierre, J.-L. Ravanat, *Chem. Res. Toxicol.* **2014**, *27*, 1011.
[7] A. M. Fleming, E. I. Armentrout, J. Zhu, J. G. Muller, C. J. Burrows, *J. Org. Chem.* **2015**, *80*, 711.
[8] K. L. Nguyen, M. Steryo, K. Kurbanyan, K. M. Nowitzki, S. M. Butterfield, S. R. Ward, E. D. A. Stemp, *J. Am. Chem. Soc.* **2000**, *122*, 3585.
[9] A. L. Madison, Z. A. Perez, P. To, T. Maisonet, E. V. Rios, Y. Trejo, C. Ochoa-Paniagua, A. Reno, E. D. A. Stemp, *Biochem.* **2012**, *51*, 362.
[10] G. Pratviel, B. Meunier, *Chem. Eur. J.* **2006**, *12*, 6018.
[11] X. Xu, J. G. Muller, Y. Ye, C. J. Burrows, *J. Am. Chem. Soc.* **2008**, *130*, 703.
[12] M. M. Moe, J. Benny, V. Lee, M. Tsai, J. Liu, *Nucleic Acids Res.* **2025**, *53*, gkaf071.
[13] N. R. Jena, P. C. Mishra, *J. Phys. Chem. B* **2007**, *111*, 5418.
[14] V. Labet, C. Morell, A. Grand, J. Cadet, P. Cimino, V. Barone, *Org. Biomol. Chem.* **2008**, *6*, 3300.
[15] B. Thapa, B. H. Munk, C. J. Burrows, H. B. Schlegel, *Chem. Res. Toxicol.* **2016**, *29*, 1396.
[16] B. Thapa, S. P. Hebert, B. H. Munk, C. J. Burrows, H. B. Schlegel, *J. Phys. Chem. A* **2019**, *123*, 5150.
[17] E. Bignon, C.-H. Chan, C. Morell, A. Monari, J.-L. Ravanat, E. Dumont, *Chem. Eur. J.* **2017**, *23*, 12845.
[18] C.-H. Chan, A. Monari, J.-L. Ravanat, E. Dumont, *Phys. Chem. Chem. Phys.* **2019**, *21*, 23418.
[19] J. Cadet, T. Douki, D. Gasparutto, J.-L. Ravanat, *Mutation Res.* **2003**, *531*, 5.
[20] W. L. Neeley, J. M. Essigmann, *Chem. Res. Toxicol.* **2006**, *19*, 491.
[21] A. M. Fleming, C. J. Burrows, *DNA Repair* **2017**, *56*, 75.
[22] ESCODD, C. M. Gedik, A. Collins, *FASEB J.* **2005**, *19*, 82.
[23] S. Steenken, S. V. Jovanovic, M. Bietti, K. Bernhard, *J. Am. Chem. Soc.* **2000**, *122*, 2373.
[24] S. Steenken, S. V. Jovanovic, *J. Am. Chem. Soc.* **1997**, *119*, 617.
[25] C. J. Burrows, J. G. Muller, *Chem. Rev.* **1998**, *98*, 1109.
[26] B. H. Munk, C. J. Burrows, H. B. Schlegel, *J. Am. Chem. Soc.* **2008**, *130*, 5245.
[27] A. M. Fleming, J. G. Muller, A. C. Dlouhy, C. J. Burrows, *J. Am. Chem. Soc.* **2012**, *134*, 15091.
[28] A. M. Fleming, C. J. Burrows, *Org. Biomol. Chem.* **2017**, *15*, 8341.
[29] M. E. Hosford, J. G. Muller, C. J. Burrows, *J. Am. Chem. Soc.* **2004**, *126*, 9540.
[30] B. Thapa, B. H. Munk, C. J. Burrows, H. B. Schlegel, *Chem. Eur. J.* **2017**, *23*, 5804.
[31] Y. Ye, J. G. Muller, W. Luo, C. L. Mayne, A. J. Shallop, R. A. Jones, C. J. Burrows, *J. Am. Chem. Soc.* **2003**, *125*, 13926.
[32] M. E. Johansen, J. G. Muller, X. Xu, C. J. Burrows, *Biochem.* **2005**, *44*, 5660.
[33] M. J. Solivio, D. B. Nemera, L. Sallans, E. J. Merino, *Chem. Res. Toxicol.* **2012**, *25*, 326.
[34] Y. Sun, M. Tsai, W. Zhou, W. Lu, J. Liu, *J. Phys. Chem. B* **2019**, *123*, 10410.
[35] X. Xu, A. M. Fleming, J. G. Muller, C. J. Burrows, *J. Am. Chem. Soc.* **2008**, *130*, 10080.
[36] J. Bai, Y. Zhang, Z. Xi, M. M. Greenberg, C. Zhou, *Chem. Res. Toxicol.* **2018**, *31*, 1364.
[37] A. Kupan, A. Saulière, S. Broussy, C. Seguy, G. Pratviel, B. Meunier, *ChemBioChem* **2006**, *7*, 125.
[38] R. P. Hickerson, C. L. Chepanoske, S. D. Williams, S. S. David, C. J. Burrows, *J. Am. Chem. Soc.* **1999**, *121*, 9901.
[39] R. P. Hickerson, F. Prat, J. G. Muller, C. S. Foote, C. J. Burrows, *J. Am. Chem. Soc.* **1999**, *121*, 9423.
[40] Z. Cai, M. D. Sevilla, *Radiat. Res.* **2003**, *159*, 411.
[41] M. M. Moe, M. Tsai, J. Liu, *ChemPlusChem* **2021**, *86*, 1243.
[42] M. D. Koppang, M. Witek, J. Blau, G. M. Swain, *Anal. Chem.* **1999**, *71*, 1188.
[43] S. J. Culp, B. P. Cho, F. F. Kadlubar, F. E. Evans, *Chem. Res. Toxicol.* **1989**, *2*, 416.
[44] J. Reynisson, S. Steenken, *J. Mol. Struct.: Theochem* **2005**, *723*, 29.
[45] Y. Fang, J. Liu, *J. Phys. Chem. A* **2009**, *113*, 11250.
[46] R. D. Levine, R. B. Bernstein, *Molecular Reaction Dynamics and Chemical Reactivity*, Oxford University Press, New York, **1987**.
[47] J. Liu, B. van Devener, S. L. Anderson, *J. Chem. Phys.* **2002**, *116*, 5530.
[48] S. J. Baek, K.-W. Choi, Y. S. Choi, S. K. Kim, *J. Chem. Phys.* **2003**, *118*, 11040.

[49] Y. Guo, C. Riplinger, U. Becker, D. G. Liakos, Y. Minenkov, L. Cavallo, F. Neese, *J. Chem. Phys.* **2018**, *148*, 011101.
[50] J. Zhou, O. Kostko, C. Nicolas, X. Tang, L. Belau, M. S. de Vries, M. Ahmed, *J. Phys. Chem. A* **2009**, *113*, 4829.
[51] E. P. Hunter, S. G. Lias, *J. Phys. Chem. Ref. Data* **1998**, *27*, 413.
[52] J. Troe, *Chem. Phys. Lett.* **1985**, *122*, 425.
[53] C. Larriba, C. J. Hogan, Jr., *J. Comput. Phys.* **2013**, *251*, 344.
[54] C. Larriba-Andaluz, C. J. Hogan, Jr., *J. Chem. Phys.* **2014**, *141*, 194107.
[55] A. Kumar, M. D. Sevilla, *J. Phys. Chem. B* **2014**, *118*, 5453.
[56] R. A. Marcus, *J. Chem. Phys.* **1952**, *20*, 359.
[57] M. Bonifačić, D. A. Armstrong, I. Štefanić, K.-D. Asmus, *J. Phys. Chem. B* **2003**, *107*, 7268.
[58] E. Wigner, *Z. physik. Chem.* **1932**, *B19*, 203.
[59] R. K. O. Sigel, E. Freisinger, B. Lippert, *J. Biol. Inorg. Chem.* **2000**, *5*, 287.
[60] L. Feketeová, E. Yuriev, J. D. Orbell, G. N. Khairallah, R. A. J. O'Hair, *Int. J. Mass Spectrom.* **2011**, *304*, 74.
[61] P. Cheng, D. K. Bohme, *J. Phys. Chem. B* **2007**, *111*, 11075.
[62] A. Dang, Y. Liu, F. Tureček, *J. Phys. Chem. A* **2019**, *123*, 3272.
[63] Y. Sun, M. Tsai, M. M. Moe, J. Liu, *J. Phys. Chem. A* **2021**, *125*, 1564.
[64] P. B. Armentrout, *J. Anal. At. Spectrom.* **2004**, *19*, 571.
[65] P. J. Chantry, *J. Chem. Phys.* **1971**, *55*, 2746.
[66] C. Lifshitz, *Eur. J. Mass Spectrom.* **2002**, *8*, 85.
[67] M. J. Frisch, G. W. Trucks, H. B. Schlegel, G. E. Scuseria, M. A. Robb, J. R. Cheeseman, G. Scalmani, V. Barone, G. A. Petersson, H. Nakatsuji, X. Li, M. Caricato, A. V. Marenich, J. Bloino, B. G. Janesko, R. Gomperts, B. Mennucci, H. P. Hratchian, J. V. Ortiz, A. F. Izmaylov, J. L. Sonnenberg, D. Williams-Young, F. Ding, F. Lipparini, F. Egidi, J. Goings, B. Peng, A. Petrone, T. Henderson, D. Ranasinghe, V. G. Zakrzewski, J. Gao, N. Rega, G. Zheng, W. Liang, M. Hada, M. Ehara, K. Toyota, R. Fukuda, J. Hasegawa, M. Ishida, T. Nakajima, Y. Honda, O. Kitao, H. Nakai, T. Vreven, K. Throssell, J. A. Montgomery Jr., J. E. Peralta, F. Ogliaro, M. J. Bearpark, J. J. Heyd, E. N. Brothers, K. N. Kudin, V. N. Staroverov, T. A. Keith, R. Kobayashi, J. Normand, K. Raghavachari, A. P. Rendell, J. C. Burant, S. S. Iyengar, J. Tomasi, M. Cossi, J. M. Millam, M. Klene, C. Adamo, R. Cammi, J. W. Ochterski, R. L. Martin, K. Morokuma, O. Farkas, J. B. Foresman, D. J. Fox, Gaussian 16 Gaussian, Inc., Wallingford, CT, **2016**, vol. Rev. D.01.
[68] I. M. Alecu, J. Zheng, Y. Zhao, D. G. Truhlar, *J. Chem. Theory Comput.* **2010**, *6*, 2872.
[69] E. D. Glendening, J. K. Badenhoop, A. E. Reed, J. E. Carpenter, J. A. Bohmann, C. M. Morales, C. R. Landis, F. Weinhold, NBO 6.0, Theoretical Chemistry Institute, University of Wiscosin, Madison, WI, **2013**.
[70] F. Neese, *WIREs Comput. Molec. Sci.* **2022**, *12*, e1606.
[71] L. Zhu, W. L. Hase, A General RRKM Program (QCPE 644), Quantum Chemistry Program Exchange, Chemistry Department, University of Indiana, Bloomington, **1993**.

Table of Contents graphic

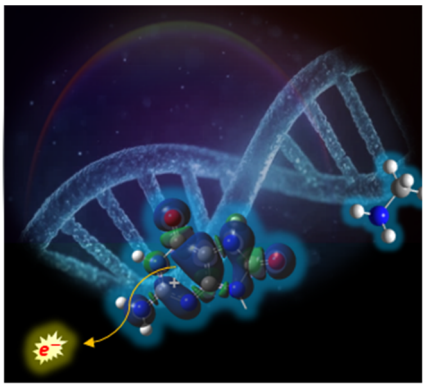

8-Oxoguanine (OG) is a common DNA lesion. Guided-ion-beam mass spectrometry experiment and computation show that one-electron-oxidized $OG^{\bullet+}$ radical cations can develop DNA–protein crosslinks (DPCs), and energy-dependent DPC pathways differ from those commonly mediated by two-electron-oxidized OG^{OX}. The results broaden our understanding of OG lesions and their biological implications.